



**University of
Zurich**^{UZH}

**Zurich Open Repository and
Archive**

University of Zurich
University Library
Strickhofstrasse 39
CH-8057 Zurich
www.zora.uzh.ch

Year: 2017

Nexus fermions in topological symmorphic crystalline metals

Chang, Guoqing ; Xu, Su-Yang ; Huang, Shin-Ming ; Sanchez, Daniel S ; Hsu, Chuang-Han ; Bian, Guang ; Yu, Zhi-Ming ; Belopolski, Ilya ; Alidoust, Nasser ; Zheng, Hao ; Chang, Tay-Rong ; Jeng, Horng-Tay ; Yang, Shengyuan A ; Neupert, Titus ; Lin, Hsin ; Hasan, M Zahid

DOI: <https://doi.org/10.1038/s41598-017-01523-8>

Posted at the Zurich Open Repository and Archive, University of Zurich

ZORA URL: <https://doi.org/10.5167/uzh-141674>

Journal Article

Published Version



The following work is licensed under a Creative Commons: Attribution 4.0 International (CC BY 4.0) License.

Originally published at:

Chang, Guoqing; Xu, Su-Yang; Huang, Shin-Ming; Sanchez, Daniel S; Hsu, Chuang-Han; Bian, Guang; Yu, Zhi-Ming; Belopolski, Ilya; Alidoust, Nasser; Zheng, Hao; Chang, Tay-Rong; Jeng, Horng-Tay; Yang, Shengyuan A; Neupert, Titus; Lin, Hsin; Hasan, M Zahid (2017). Nexus fermions in topological symmorphic crystalline metals. *Scientific Reports*, 7:1688.

DOI: <https://doi.org/10.1038/s41598-017-01523-8>

SCIENTIFIC REPORTS

OPEN

Nexus fermions in topological symmorphic crystalline metals

Guoqing Chang^{1,2}, Su-Yang Xu³, Shin-Ming Huang⁴, Daniel S. Sanchez³, Chuang-Han Hsu^{1,2}, Guang Bian³, Zhi-Ming Yu^{5,6}, Ilya Belopolski³, Nasser Alidoust³, Hao Zheng³, Tay-Rong Chang⁷, Horng-Tay Jeng^{7,8}, Shengyuan A. Yang⁶, Titus Neupert^{9,10}, Hsin Lin^{1,2} & M. Zahid Hasan³

Received: 19 September 2016

Accepted: 17 February 2017

Published online: 10 May 2017

Topological metals and semimetals (TMs) have recently drawn significant interest. These materials give rise to condensed matter realizations of many important concepts in high-energy physics, leading to wide-ranging protected properties in transport and spectroscopic experiments. It has been well-established that the known TMs can be classified by the dimensionality of the topologically protected band degeneracies. While Weyl and Dirac semimetals feature zero-dimensional points, the band crossing of nodal-line semimetals forms a one-dimensional closed loop. In this paper, we identify a TM that goes beyond the above paradigms. It shows an exotic configuration of degeneracies without a well-defined dimensionality. Specifically, it consists of 0D nexus with triple-degeneracy that interconnects 1D lines with double-degeneracy. We show that, because of the novel form of band crossing, the new TM cannot be described by the established results that characterize the topology of the Dirac and Weyl nodes. Moreover, triply-degenerate nodes realize emergent fermionic quasiparticles not present in relativistic quantum field theory. We present materials candidates. Our results open the door for realizing new topological phenomena and fermions including transport anomalies and spectroscopic responses in metallic crystals with nontrivial topology beyond the Weyl/Dirac paradigm.

Understanding nontrivial topology in gapless materials including metals and semimetals has recently emerged as one of the most exciting frontiers in the research of condensed matter physics and materials science^{1–17}. Unlike conventional metals, topological metals/semimetals (TMs) are materials whose Fermi surface arises from the degeneracy of conduction and valence bands, which cannot be avoided due to their nontrivial topology. To date, the known TMs include Dirac semimetals, Weyl semimetals, and nodal-line semimetals. Dirac or Weyl semimetals have zero-dimensional (0D) band crossings, i.e., the Dirac or Weyl nodes and a Fermi surface that consists of isolated 0D points in the bulk Brillouin zone (BZ). By contrast, nodal-line semimetals feature one-dimensional (1D) band crossings and a Fermi surface that is made up of 1D closed loops in the BZ. Therefore, the band crossings serve as a key signature of nontrivial topology in metals and can be used to classify TMs. More importantly, these band crossings can give rise to fundamentally new physical phenomena. Since low-energy excitations near the Dirac or Weyl nodes mimic elementary fermions, TMs provide a unique opportunity to study important concepts of high-energy physics such as Dirac fermions, Weyl fermions, and the chiral anomaly in table-top experiments. The correspondence with high-energy physics, in turn, leads to a cornucopia of topologically protected phenomena. The resulting key experimental detectable signatures include the Dirac, Weyl or nodal-line quasiparticles in the bulk, the Fermi arc or drumhead topological surface states on the boundaries, the negative magnetoresistance and nonlocal transport induced by the chiral anomaly^{18,19}, the surface-to-surface quantum

¹Centre for Advanced 2D Materials and Graphene Research Centre National University of Singapore, 6 Science Drive 2, Singapore, 117546, Singapore. ²Department of Physics, National University of Singapore, 2 Science Drive 3, Singapore, 117542, Singapore. ³Laboratory for Topological Quantum Matter and Spectroscopy (B7), Department of Physics, Princeton University, Princeton, New Jersey, 08544, USA. ⁴Department of Physics, National Sun Yat-sen University, Kaohsiung, 80424, Taiwan. ⁵School of Physics, Beijing Institute of Technology, Beijing, 100081, China. ⁶Research Laboratory for Quantum Materials, Singapore University of Technology and Design, Singapore, 487372, Singapore. ⁷Department of Physics, National Tsing Hua University, Hsinchu, 30013, Taiwan. ⁸Institute of Physics, Academia Sinica, Taipei, 11529, Taiwan. ⁹Princeton Center for Theoretical Science, Princeton University, Princeton, New Jersey, 08544, USA. ¹⁰Department of Physics, University of Zurich, Winterthurerstrass, 190, CH-8052, Switzerland. Guoqing Chang and Su-Yang Xu contributed equally to this work. Correspondence and requests for materials should be addressed to S.-Y.X. (email: suyangxu@princeton.edu) or H.L. (email: nilnish@gmail.com) or M.Z.H. (email: mzhasan@princeton.edu)

oscillation due to Fermi arcs^{20,21}, the Kerr and Faraday rotations in optical experiments²², and topological superconductivity and Majorana fermions when superconductivity is induced via doping or proximity effect^{23–26}. Because all these fascinating properties arise from the band crossings, there has been growing interest in the search for new TMs with new types of band crossings^{27,28}, including a classification of 3-, 6-, and 8-fold band degeneracies that appear at high-symmetry points in non-symmorphic crystals²⁸. Such efforts can lead to new protected phenomena in transport and spectroscopic experiments, which can be potentially utilized in device applications.

In this paper, we identify a class of TMs featuring a type of band crossing beyond the Dirac, Weyl and nodal-line cases. Specifically, we find that the new TM features a pair of triply-degenerate nodes, which are interconnected by multi-segments of lines with two-fold degeneracy. The triply-degenerate node realizes emergent fermionic quasiparticles beyond the Dirac and Weyl fermions in quantum field theory. Moreover, the new band crossing evades the classification of TMs based dimensionality because it is neither 0D nor 1D but rather a hybrid. We show that this band crossing gives rise to a distinct Landau level spectrum, suggesting novel magneto-transport responses. Further, we identify the space groups, in which this new TM state can occur and present material candidates for each space group. Our results highlight the exciting possibilities to realize new particles beyond high-energy textbook examples and to search for new topologically protected low-energy phenomena in transport and spectroscopic experiments beyond the Weyl/Dirac paradigm.

Theory of the new band crossing

We first present a physical picture of the new band crossing without going into mathematical details. We consider an inversion breaking crystal lattice with a three-fold rotational symmetry along the \hat{z} direction (\tilde{C}_{3z}) and a mirror symmetry that sends $x \rightarrow -x$ (\tilde{M}_x). Note that the \tilde{C}_{3z} rotational symmetry replicates the \tilde{M}_x twice. In momentum space there are thus in total three mirror planes intersecting along the k_z axis as shown in Fig. 1a,b. We first consider the case without spin-orbit coupling (SOC). The \tilde{C}_{3z} operator has three eigenvalues, namely, $e^{-i\frac{2\pi}{3}}$, $e^{i\frac{2\pi}{3}}$, and 1, and we denote the corresponding eigenstates as ψ_1 , ψ_2 , and ψ_3 , respectively. Under the mirror reflection \tilde{M}_x , ψ_3 remains unchanged ($\tilde{M}_x\psi_3 = \psi_3$), whereas ψ_1 and ψ_2 will transform into each other ($\tilde{M}_x\psi_1 = \psi_2$; $\tilde{M}_x\psi_2 = \psi_1$). Thus \tilde{C}_{3z} and \tilde{M}_x do not commute and cannot be simultaneously diagonalized in the space spanned by ψ_1 and ψ_2 . Both \tilde{C}_{3z} and \tilde{M}_x leave every momentum point along the k_z axis invariant. Thus, at each point along the k_z axis, the Bloch states that form a possibly degenerate eigenspace (band) of the Hamiltonian must be invariant under both \tilde{C}_{3z} and \tilde{M}_x . Failure of \tilde{C}_{3z} and \tilde{M}_x to be simultaneously diagonalizable thus enforces a two-fold band degeneracy of bands with the same eigenvalues as ψ_1 and ψ_2 . Therefore, in the absence of SOC, along the k_z axis, the three bands with the three different \tilde{C}_{3z} eigenvalues always appear as a singly-degenerate band (ψ_3) and a doubly-degenerate band (ψ_1 and ψ_2). If the single degenerate and the doubly-degenerate bands cross each other accidentally, a triply-degenerate node will form because their different \tilde{C}_{3z} eigenvalues prohibit hybridization.

When spin is added to the picture, all bands discussed above gain an additional double degeneracy in absence of SOC. However, SOC generically lifts the resulting 6-fold degeneracy into two three-fold degeneracies in absence of inversion symmetry away from the time-reversal symmetric momenta. These three-fold degeneracies are protected for very similar reasons as in the spinless case. The three eigenvalues of the spinful C_{3z} operator are $e^{-i\frac{2\pi}{3}}$, $e^{i\frac{2\pi}{3}}$, and $e^{i\pi}$. The same symmetry argument combining C_{3z} and the spinful mirror operator \mathcal{M}_x will show that the two states with $e^{\pm i\frac{2\pi}{3}}$ eigenvalues must be degenerate. Considering all these conditions collectively, the six bands appear as two singly-degenerate bands with the C_{3z} eigenvalue of $e^{i\pi}$ and two doubly-degenerate bands with the C_{3z} eigenvalues of $e^{\pm i\frac{2\pi}{3}}$. An accidental crossing between a singly-degenerate and a doubly-degenerate band will give rise to a triply-degenerate node along the k_z axis. Away from the k_z axis, all of the three bands can hybridize and the degeneracies will be lifted. Along the k_z axis, a two-fold degenerate nodal line emanates from the three-fold degeneracy, but this degeneracy occurs between the lowest and the middle band on one side of the three-fold degeneracy and between the middle and the highest band on the other side. This structure of degeneracies is reminiscent of but yet distinct from the three-fold degeneracy found for space group 220 in ref. 28, where pairs of nodal lines emanate from a three-fold degenerate point. The latter is pinned to a high-symmetry point and the symmetries realizing it are quite different from the scenario discussed here.

Now we present the effective Hamiltonian near the triply-degenerate node. In the presence of spin-orbit coupling, we denote three eigenstates of C_{3z} with the eigenvalues of $e^{-i\frac{2\pi}{3}}$, $e^{i\frac{2\pi}{3}}$, and $e^{i\pi}$ as ψ'_1 , ψ'_2 and ψ'_3 , respectively. Using the basis $(\psi'_1, \psi'_2, \psi'_3)$, the C_{3z} and \mathcal{M}_x operators have the representations

$$C_{3z} = \begin{pmatrix} e^{i\frac{2\pi}{3}} & 0 & 0 \\ 0 & e^{-i\frac{2\pi}{3}} & 0 \\ 0 & 0 & -1 \end{pmatrix}, \mathcal{M}_x = \begin{pmatrix} 0 & i & 0 \\ i & 0 & 0 \\ 0 & 0 & i \end{pmatrix}, \quad (1)$$

It can be seen that C_{3z} and \mathcal{M}_x do not commute with each other, ψ'_1 and ψ'_2 form a two-dimensional irreducible representation. Therefore, ψ'_1 and ψ'_2 have to be degenerate at all k points along the k_z axis. We present a $k \cdot p$ model for the bands in the vicinity of one triply-degenerate fermion. We denote the momentum relative to the triply-degenerate node as $\mathbf{q} = (q_x, q_y, q_z)$. The $k \cdot p$ Hamiltonian to linear order in q_z and quadratic order q_x and q_y can be written as

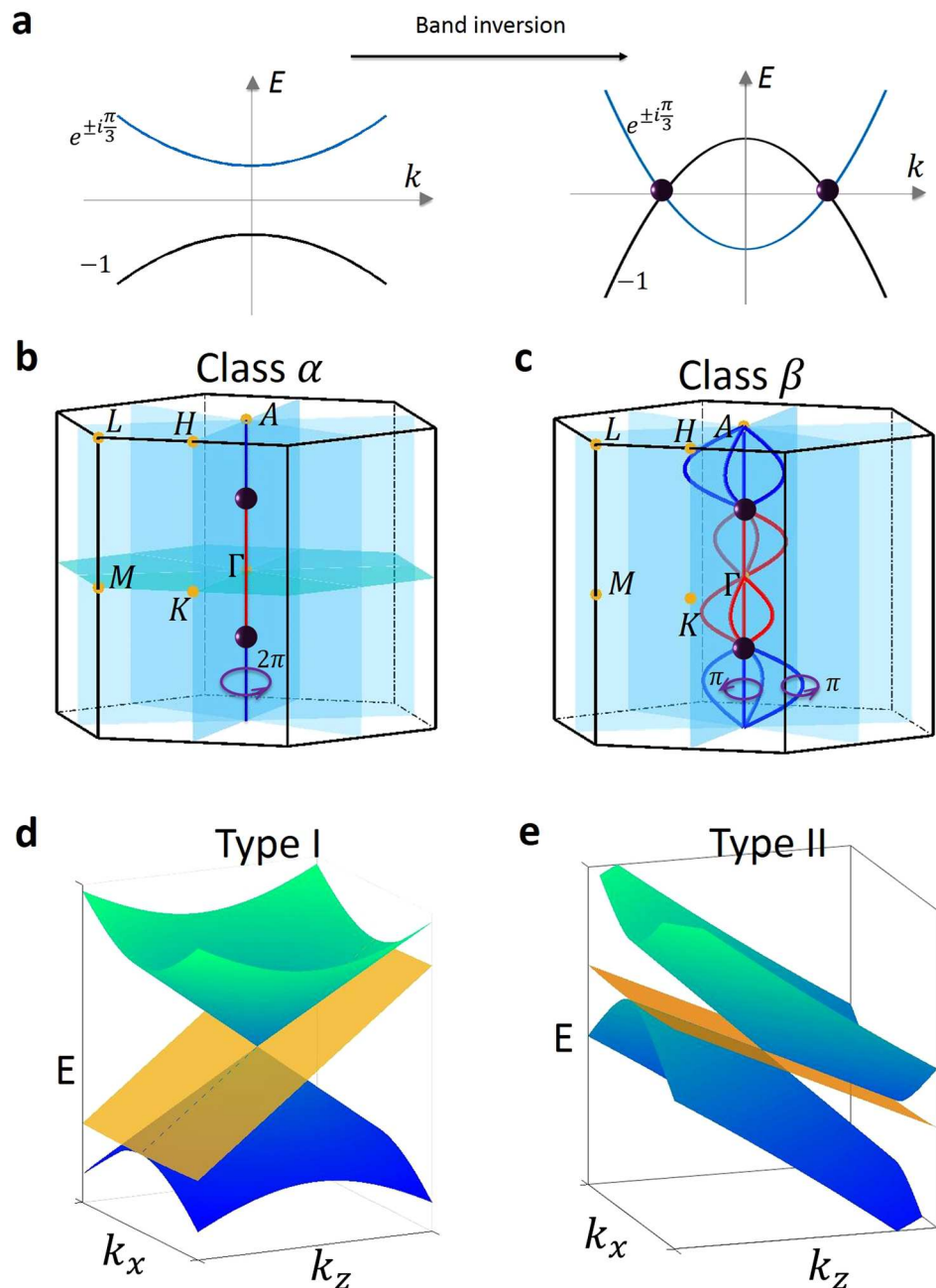


Figure 1. Band crossings in the new topological metal. (a) Cartoon illustration to visualize the band inversion process that drives a three-fold band crossing, which generates a pair of triply-degenerate nodes (purple spheres). In the weak hopping limit (left panel), electrons can hardly hop from one atomic site to the other. Therefore, the dispersion of bands is very weak. The doubly-degenerate band (blue) and singly-degenerate band (black) are separated by a band gap. (Labels $e^{\pm i\pi/3}$, 1 are rotation eigenvalues). As the magnitude of hopping is increased, bands will gain stronger dispersion. When the band width is large enough, the two bands will be inverted in some k region of the BZ and cross each other at two points on the opposite sides of the Γ point along the k_z axis. These two crossings are the triply-degenerate nodes. (b,c) Cartoon showcasing the two distinct classes of the new band crossings: Class α and Class β . The bulk Brillouin zones are represented with the relevant high symmetry points (yellow dots), $k_z=0$ mirror plane (turquoise) and three mirror-symmetric planes (blue) along the C_{3z} -axis. In Class α , all of the band crossings reside on the k_z -axis. A pair of triply-degenerate nodes are connected by non-closed 1D segments with two-fold degeneracy. A trivial 2π Berry phase was computed along a closed loop around the open segment. In Class β , the two-fold degenerate band crossing form closed contours, which allows for a non-trivial π Berry phase to be defined. (d,e) A cartoon illustrating the two types of allowed band dispersions for triply-degenerate nodes: type-I and type-II. Type-I is described by a linear dispersion for both the doubly- and singly-degenerate bands. Type-II is described by band dispersions with the same Fermi velocity direction along k_z for both the doubly- and singly-degenerate bands.

$$H(\mathbf{q}) = tq_z + \begin{pmatrix} \Delta_t q_z & \lambda q_+^2 + i\lambda_R q_- & \lambda'^* q_+ \\ \lambda q_-^2 - i\lambda_R q_+ & \Delta_t q_z & -\lambda' q_- \\ \lambda' q_- & -\lambda' q_+ & -\Delta_t q_z \end{pmatrix}, \quad (2)$$

where $q_{\pm} = q_x \pm iq_y$, the parameters t , Δ_t , λ and λ_R are real, and λ' is a complex parameter. We now explain how the three-fold band crossing can arise through a band inversion process. Consider a material whose lowest valence and conduction bands are the singly-degenerate band (ψ_3') and the doubly-degenerate band (ψ_1' and ψ_2'), respectively. As shown in Fig. 1a, if we turn off the hopping of electrons between atomic sites (this can be conceptually done by increasing the lattice constants to infinity), then all bands are flat and the system is an insulator. Now as we gradually increase the magnitude of hopping (this can be conceptually done by decreasing the lattice constant from infinity), bands will gain dispersion. When the band width is large enough relative to the energy offset between the bands, the two bands will be inverted in some interval along the k_z axis (Fig. 1a) and cross each other at two points on the opposite sides of the Γ point along the k_z axis. These two crossings are the triply-degenerate nodes. This process shows that the triply-degenerate nodes in our new TM always come in pairs and they can move along the k_z axis as the band dispersion is varied.

We find that the new band crossing can be classified into two classes, namely Class α and Class β , depending on whether the mirror symmetry \mathcal{M}_z is present (Class α) or not (Class β). (On the level of the effective Hamiltonian (2), \mathcal{M}_z enforces that λ' is real and $\lambda_R = 0$). The momentum configurations of band degeneracies in both classes are shown in Fig. 1b,c, respectively. They differ in the line degeneracies that connect the triply-degenerate nodes. In Class α , the energy eigenvalues are

$$\varepsilon_1 = tq_z + \Delta_t q_z + \lambda |q_+|^2, \quad \varepsilon_{2,3} = tq_z - \frac{1}{2}\lambda |q_+|^2 \pm \sqrt{2\lambda'^2 |q_+|^2 + (\Delta_t q_z - \frac{1}{2}\lambda |q_+|^2)^2}, \quad (3)$$

two of which are degenerate on the k_z axis. Specifically, two isolated triply-degenerate nodes are located on the opposite sides of the Γ point, which arise from the degeneracy between all three (ψ_1' , ψ_2' and ψ_3') bands. These two triply-degenerate nodes are linked by non-closed 1D segments with two-fold degeneracy, which arise from the degeneracy between the ψ_1' , ψ_2' bands. At any generic k point on the two-fold degenerate segments, the in-plane (k_x or k_y) dispersion is a quadratic touching of the ψ_1' , ψ_2' bands. The Berry phase along a closed loop around the open segment is 2π , which is trivial. By contrast, in Class β , the two-fold degenerate 1D band crossings form four strands at every cut of constant k_z that join at the triply-degenerate nodes. At any generic k point on the two-fold degenerate lines, the in-plane (k_x or k_y) dispersion is a linear touching of the ψ_1' , ψ_2' bands, and the Berry phase around each line is $\pm\pi$, which is nontrivial. One of the four two-fold degenerate segments is pinned to align with the k_z axis. The distinction between Class α and Class β can be understood by an analogy between the Hamiltonian at a generic slice of constant k_z with both real-space nexus in 3He-A^{29,30} and momentum space nexus of bilayer graphene^{30,31}. In the bilayer graphene, the addition of skew interlayer hopping turns a quadratic band touching, corresponding to one degeneracy line segment in Class α , into a quadruplet of Dirac points, corresponding four degeneracy line segments in Class β ³¹. However, an important difference is that the bands described by this effective Hamiltonian in graphene are doubly degenerate due to spin, while the effective model for the triply degenerate fermion already includes spin-orbit coupling, and therefore describes bands without residual degeneracies.

We can further classify the triply-degenerate node by its band dispersion into type-I and type-II, in analogy to a recently introduced notion for Weyl semimetals⁴¹. In our case, in type-I, the singly-degenerate band and the doubly-degenerate band have Fermi velocities of opposite sign, whereas in type-II all Fermi velocities are of the same sign along the k_z axis. The two situations are separated by a Lifschitz transition.

To explicitly reveal the novelty of the new TM, we show that the new band crossing cannot be describe by the established results in topological band theory, which have successfully characterized the topology of the Dirac and Weyl nodes. We first briefly review the established results for the Dirac/Weyl cases. A Weyl node is a point crossing between two singly degenerate bands (bands “1” and “2” in Fig. 2a). We enclose the Weyl node by a sphere in k space as shown in Figs. 2b,c. We notice that the sphere satisfies following two crucial conditions: (1) The sphere is a 2D closed manifold; (2) Bands 1 and 2 are separated by a band gap at all k points on the sphere. These two facts guarantee that one can calculate the Chern number of the filled valence bands on this sphere. Because the Weyl nodes are Berry curvature monopoles, it has been shown¹ the Chern number (C) of the sphere equals the chiral charge (χ) of the enclosed Weyl node, which serves as the topological invariant of the Weyl node. Specifically, for a single Weyl node, we have $\chi = \pm 1$ where the sign depends on the chirality of the Weyl node. For a Dirac node, we have a band crossing between two doubly-degenerate bands. Same as the Weyl node case, we can enclose the Dirac node by a sphere in k space and it is evident that the sphere will also satisfy the two conditions above, which allow the definition of a Chern number on the sphere. Because a Dirac node can be viewed as two degenerate Weyl nodes of opposite chirality, it can be shown that the chiral charge of a Dirac node is always zero, i.e., $\chi = 0$.

Now we show why this established method cannot characterize the topology of the new band crossing. As shown in Fig. 2g–i, we enclose the triply degenerate point by a sphere. Now, if we want to use the method described above, we need to find two bands that are separated by a full energy gap at all k points on this sphere. However, we see that, between bands 1 and 2, the band gap vanishes at the left-pole of the sphere (Fig. 2h). Similarly, between bands 2 and 3, the band gap is zero at the right-pole of the sphere (Fig. 2i). Therefore, due to the exotic configuration of the new band crossing, it is impossible to enclose it with a 2D closed manifold on

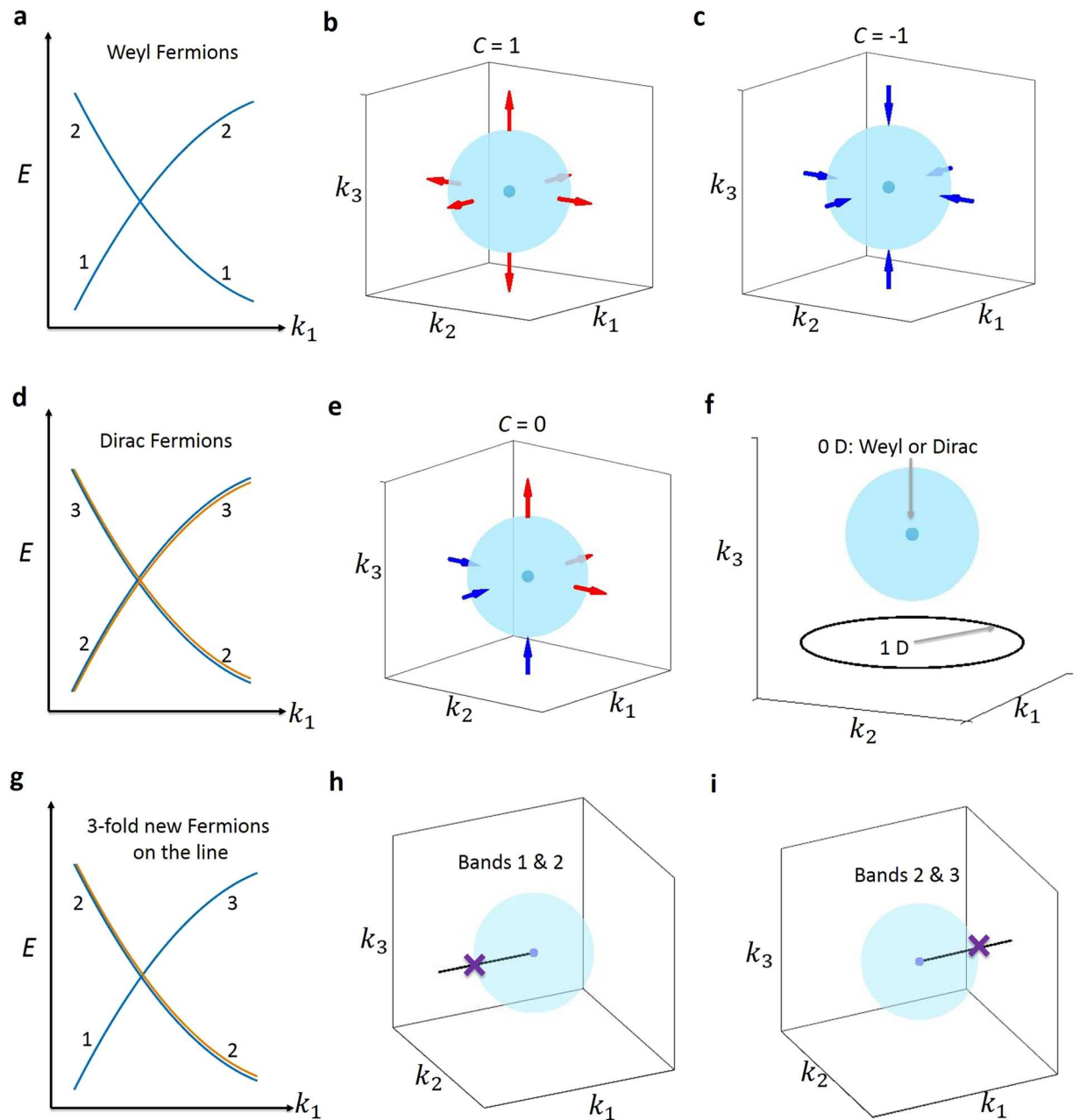


Figure 2. Comparison between Weyl, Dirac, and nexus band crossings. (a) A Weyl node arises from the crossing between two singly degenerate bands. The valence and conduction bands are noted as “1” and “2”. (b,c) We enclose the Weyl node by a sphere in k space. We notice that the sphere satisfies following two crucial conditions: (1) The sphere is a 2D closed manifold; (2) Bands 1 and 2 are separated by a band gap at all k points on the sphere. These two facts guarantee that one can calculate the Chern number of the filled valence bands on this sphere. Because the Weyl nodes are Berry curvature monopoles, it has been shown¹ the Chern number (C) of the sphere equals the chiral charge (χ) of the enclosed Weyl node, which serves as the topological invariant of the Weyl node. (d,e) A Dirac node arises from the crossing between two doubly degenerate bands (1, 2 and 3, 4). We can also enclose the Dirac node by a sphere in k space. The sphere will also satisfy the same two conditions. Because a Dirac node can be viewed as two degenerate Weyl nodes of opposite chirality, it can be shown that the chiral charge of a Dirac node is always zero, i.e., $\chi = 0$. (g–i) The new band crossing here arises from the crossing between a singly degenerate band and a doubly degenerate band. However, if we try to enclose the triply degenerate node with a sphere, we see that it is not possible to have a fully gapped band structure on the sphere. Specifically, between bands 1 and 2, the band gap vanishes at the left-pole of the sphere. Similarly, between bands 2 and 3, the band gap is zero at the right-pole of the sphere. For this reason, it is not possible to define and calculate the Chern number on the sphere as done in the Dirac/Weyl cases. (f) A trivial case where the band crossing is a simple composition of a 0D Weyl node plus a 1D nodal line.

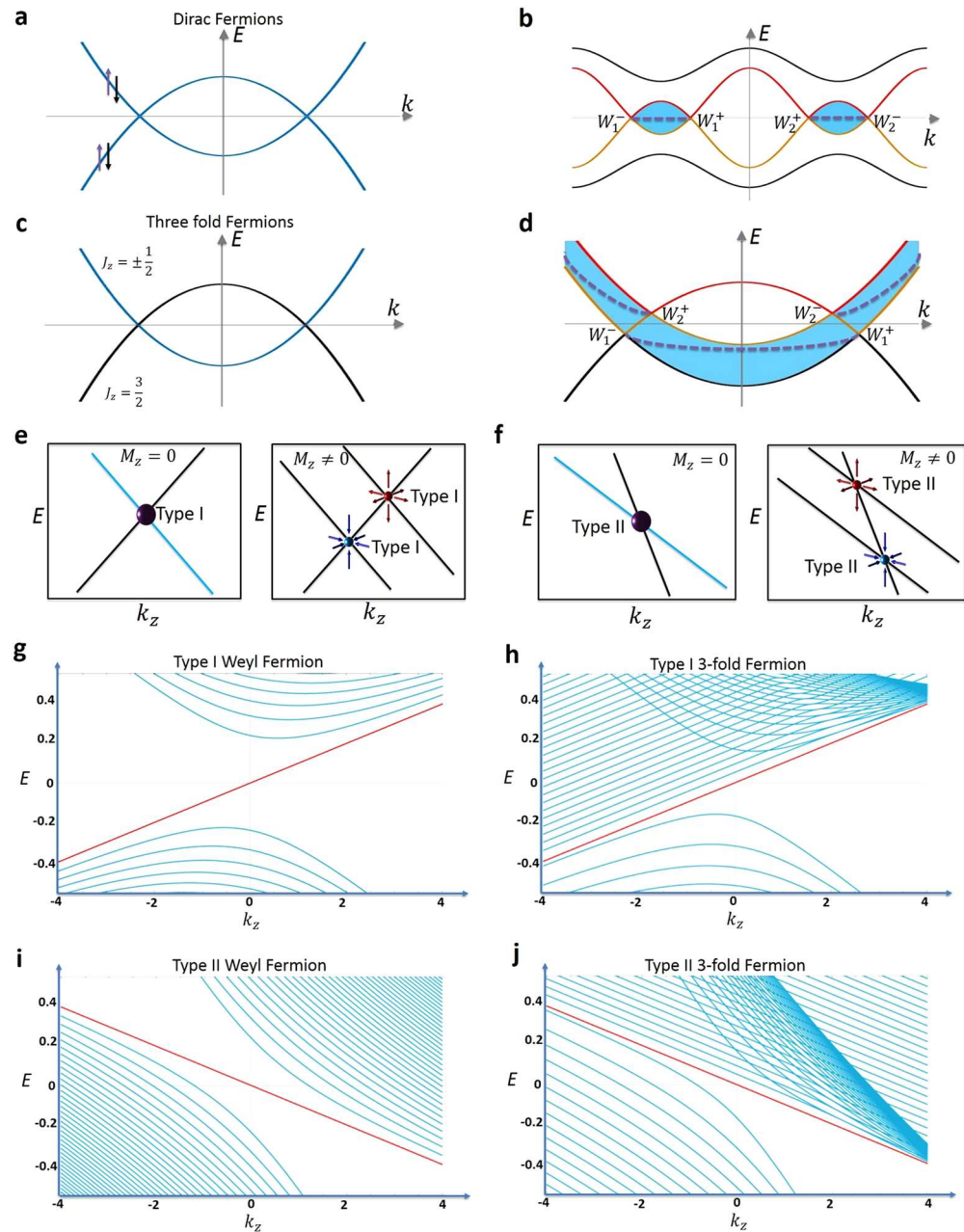


Figure 3. Zeeman coupling and Landau level spectrum. (a) Cartoon illustration of two doubly-degenerate bands crossing. The four-fold degenerate crossing point describes Dirac fermion quasiparticles. (b) In the presence of a Zeeman field, the two Dirac fermions described in (a) split into 2 pairs of Weyl fermions (i.e. $\rightarrow W_1^+ + W_1^-$). All pairs of generated Weyl fermions arise from the crossing between two singly-degenerate bands (red and yellow). The blue shaded region corresponds to section in the Brillouin zone with a non-zero Chern number. (c) Cartoon illustration of a doubly-degenerate band (blue) crossing a singly-degenerate band to create a pair of triply-degenerate fermions at the crossing points. (d) In the presence of a magnetic field, the doubly-degenerate band splits into two singly-degenerate bands, which then cross the singly-degenerate band at two different locations. Because the pair of generated Weyl fermions are not the crossing points between the same two singly-degenerate bands, the blue shaded area with a non-zero Chern number is distinctly different from the Dirac fermion case presented in (b). (e,f) A cartoon schematic for the splitting of a triply-degenerate type-I and type-II fermion (purple sphere) in the absence (left panels) and presence (right panels) of a M_z field, respectively. (g,i) Landau level spectrum for type-I (left panel) and type-II (right panel) Weyl fermions, respectively, for a magnetic field along the z direction. Type-I Weyl fermions produce a gapless chiral Landau level spectrum, and realize the chiral anomaly of quantum field theory. Type-II Weyl fermions have a gapless chiral Landau level spectrum only when the magnetic field points along certain directions, and, therefore, realize an anisotropic chiral anomaly. (h,j) Landau level spectrum for Class α triply-degenerate fermions of type-I (h) and type-II (j), respectively. The zeroth order Landau level band is in red.

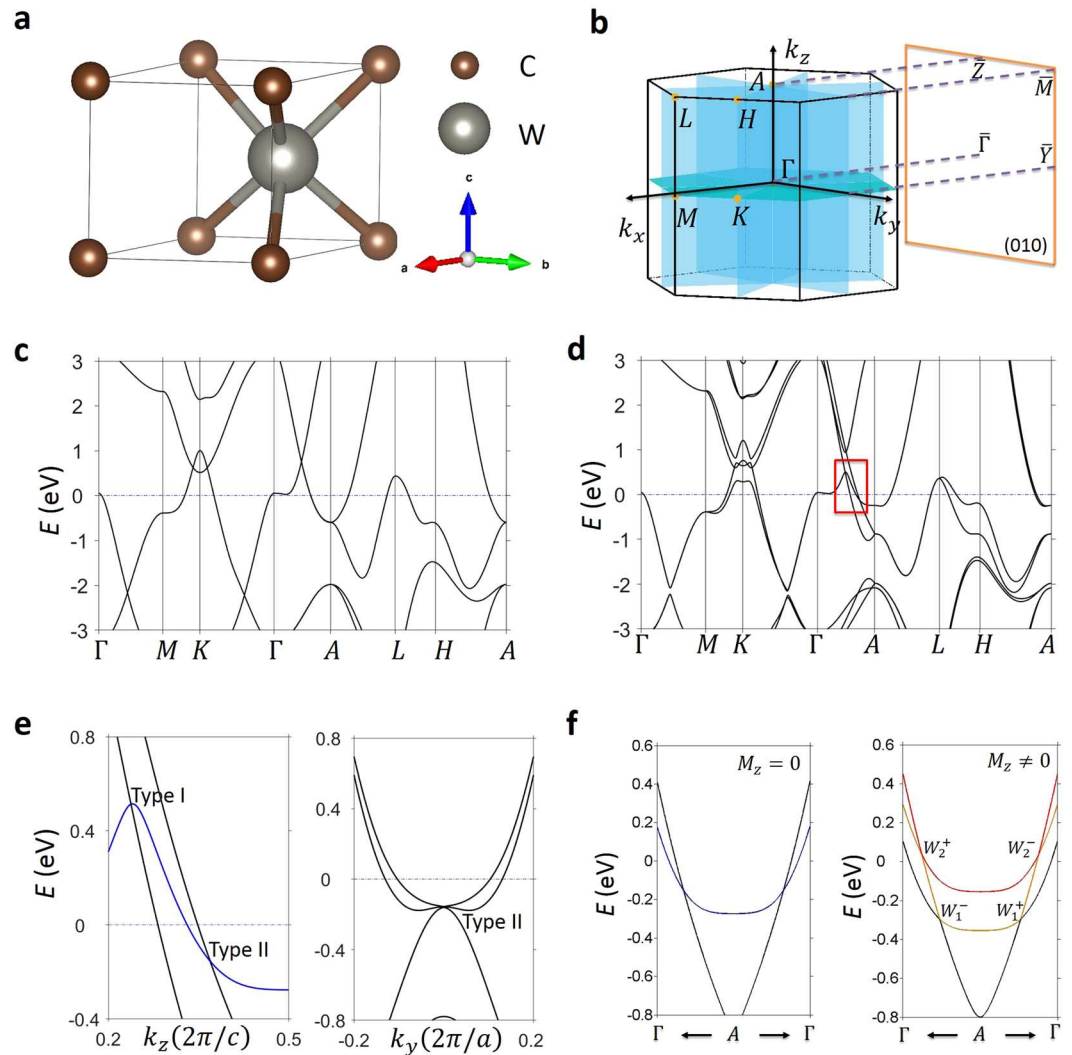


Figure 4. Material realizations of the new topological metal in WC class of materials. **(a)** Crystal structure of WC with space group $P-6m2$ (#187), showing the W and C atoms as silver and bronze spheres. **(b)** The corresponding bulk Brillouin zone with the relevant high symmetry points (yellow dots), $k_z = 0$ mirror plane (turquoise), and three mirror planes (blue) that intersect along the C_3 -axis. **(c)** Band structure calculation of WC without SOC. In the absence of SOC, the crossing along $M - K - \Gamma$ results in a nodal ring around the K point. **(d)** Same calculation as in **(c)** but with the inclusion of SOC. Enclosed in the red rectangular box are two observed crossings points along the $\Gamma - A$ line. Furthermore, inclusion of SOC allows for the touching points along $M - K - \Gamma$ that are protected by the $k_z = 0$ mirror plane to remain and form two nodal rings around the K point. **(e)** In the left panel, a zoomed-in calculation of the region within the red rectangular box in **(d)** reveals that the doubly (blue) and singly (black) degenerate bands cross at two different energies. The triply-degenerate node above the Fermi level is type-I, and the one below the Fermi level is type-II. In the right panel, the type-II character of the triply-degenerate fermion is shown by cutting through the degeneracy point along the k_a -direction. **(f)** Zoomed-in calculation of the observed type-II triply-degenerate crossing in **(e)** in the absence (left panel) and presence of a magnetic field along the k_z -direction. The application of the field along this direction preserved C_3 symmetry, and results in the triply-degenerate fermion to split into a pair of Weyl fermions by splitting the doubly-degenerate band into two singly-degenerate bands. The resulting two Weyl fermions are labeled as W_1 and W_2 , marking the crossing points between the black/yellow and red/yellow bands, respectively.

which the band structure is fully gapped. This fact demonstrates that the established results in topological band theory for the Dirac/Weyl cases cannot be used for the new band crossing. While the topological invariant for the new band crossing is an open question in theory that deserves further investigation, the fact that it cannot be described by the established results already demonstrates that it represents a breakthrough beyond the Dirac/Weyl paradigm. This fact also shows that the new band crossing cannot be viewed as a simple composition of a 0D point plus a 1D nodal line (Fig. 2f). In that case, the 0D point and the 1D nodal line are isolated with respect to each other, and each of them separately and independently admits its own topological classification. The 0D point can be enclosed by a 2D sphere whereas the 1D nodal line can be enclosed by a 1D loop. By contrast, in the new band crossing in our case, the 0D triple point serves as the connection point of the 1D nodal lines, meaning

Material	Space group	Type	Class
WC ³²	187	I and II	α
ZrTe ³³	187	I	α
δ -TaN ³⁴	187	I and II	α
NbN ³⁵	187	I and II	α
VN ³⁶	187	I and II	α
LiScl ₃ ³⁷	188	II	α
ε -TaN ³⁸	189	II	α
Li ₂ Sb ³⁹	190	II	α
AgAlS ₂ ⁴⁰	156	I and II	β
AuCd ⁴¹	157	I	β
RuCl ₃ ⁴²	158	II	β
Ge ₃ N ₄ ⁴³	159	I and II	β

Table 1. A list of candidates for the new topological metal.

that they cannot be separated. Because of this very fact, it is impossible to enclose the triple point with a 2D closed manifold on which the band structure is fully gapped so that one can define a Chern number, as we have shown above. Therefore, the exotic configuration of the new band crossing excludes a well-defined dimensionality.

Zeeman Coupling

In order to understand how the new TM responds to magnetism or magnetic doping in experiments, we study the Zeeman coupling and contrast it with Dirac semimetals. A topological Dirac semimetal system has time-reversal symmetry, space-inversion symmetry, and a uniaxial rotational symmetry along the k_z direction. The presence of time-reversal and space-inversion symmetries requires all bands to be doubly-degenerate because spin up and spin down states have the same energy (Fig. 3a). The crossing between two doubly-degenerate bands is realized by a pair of four-fold degenerate points, Dirac nodes, which are protected by the uniaxial rotational symmetry. We consider the effect of a Zeeman field in the z direction, which can be realized by a magnetization or an external magnetic field. Because the Zeeman coupling will lift the spin degeneracy, two doubly-degenerate bands become four singly-degenerate bands. However, since the bands can be distinguished by their rotation eigenvalue, protected two-fold band crossings remain, as shown in Fig. 3b. This corresponds to splitting each Dirac node into a pair of Weyl nodes with opposite chiral charge. Each blue shaded area shows the separation between the pair of Weyl nodes that arise from the splitting of a Dirac node in energy and momentum space. These areas also define the regions with non-zero Chern number. Specifically, we consider a 2D k_x, k_y slice of the BZ perpendicular to the k_z axis, and we calculate the Chern number of the band structure on such a slice for all bands below some energy E . The Chern number of the slice is only non-zero if the pair (k_z, E) lies within the blue shaded region.

The effect of Zeeman field in z direction, which breaks \mathcal{M}_x , is quite different for the new TM. As shown in Fig. 3c, the two-fold degeneracy between the ψ_1' and ψ_2' bands is lifted. As a result the doubly-degenerate (blue) band splits into two singly-degenerate bands, each of which crosses with the third band to form a Weyl node. Therefore, each triply-degenerate fermion splits into a pair of Weyl nodes with opposite chiral charge. We point out a number of key distinctions between the Dirac semimetal and the new TM cases. First, in a Dirac semimetal, the immediate pair of Weyl nodes that emerge from the same Dirac node (e.g., W_1^- and W_1^+ in Fig. 3b) arise from crossings between the same two bands (the yellow and red bands). By contrast, in the new TM, the pair of Weyl nodes that emerge from the same triply-degenerate node (e.g., W_1^- and W_2^+ in Fig. 3d) arise from the crossings between three different bands. Specifically, W_1^- is due to the crossing between the black and the yellow bands whereas W_2^+ is due to the crossing between the yellow and the red bands. As a result, the energy-momentum region with nonzero Chern number (the blue shaded area) in the new TM is drastically different from that of in a Dirac semimetal and spans across all k_z . Figures 3e,f further show how a triply-degenerate node splits into a pair of Weyl nodes under a Zeeman coupling, for the type-I and -II cases, respectively.

Landau level spectrum

In order to understand the magneto transport property of the new TM, we now compare and study the Landau level spectrum arising from triply-degenerate fermions and Weyl fermions. The application of an external magnetic field quantizes the 3D band structure into effective 1D Landau bands that disperse along the k -direction that is parallel to the field. In Fig. 3g the Landau level spectrum along the k_z is shown for a magnetic field applied along the z direction. The Weyl fermion is shown to have a gapless chiral Landau level spectrum. Specifically, besides many parabolic bands away from the Fermi level forming the conduction and valence bands, and we observe a zeroth Landau band (red) extending across the Fermi level. The sign of the velocity of the chiral zeroth Landau level is determined by the chirality of the Weyl fermion.

This is contrasted with Fig. 3h, showing the Landau level spectrum along k_z for type-I and type-II triply-degenerate fermions in the left and right panel, respectively. We first point out the similarities between the Weyl fermion and the triply-degenerate fermion cases. We see that the Landau levels found in the Weyl fermion case, i.e., the gapped Landau levels away from the Fermi level and the gapless chiral zeroth Landau level crossing the Fermi level, are also observed in the triply-degenerate fermion case. We now emphasize the differences. Essentially, we see a number of equally spaced Landau levels parallel to the zeroth (red) one, which are not

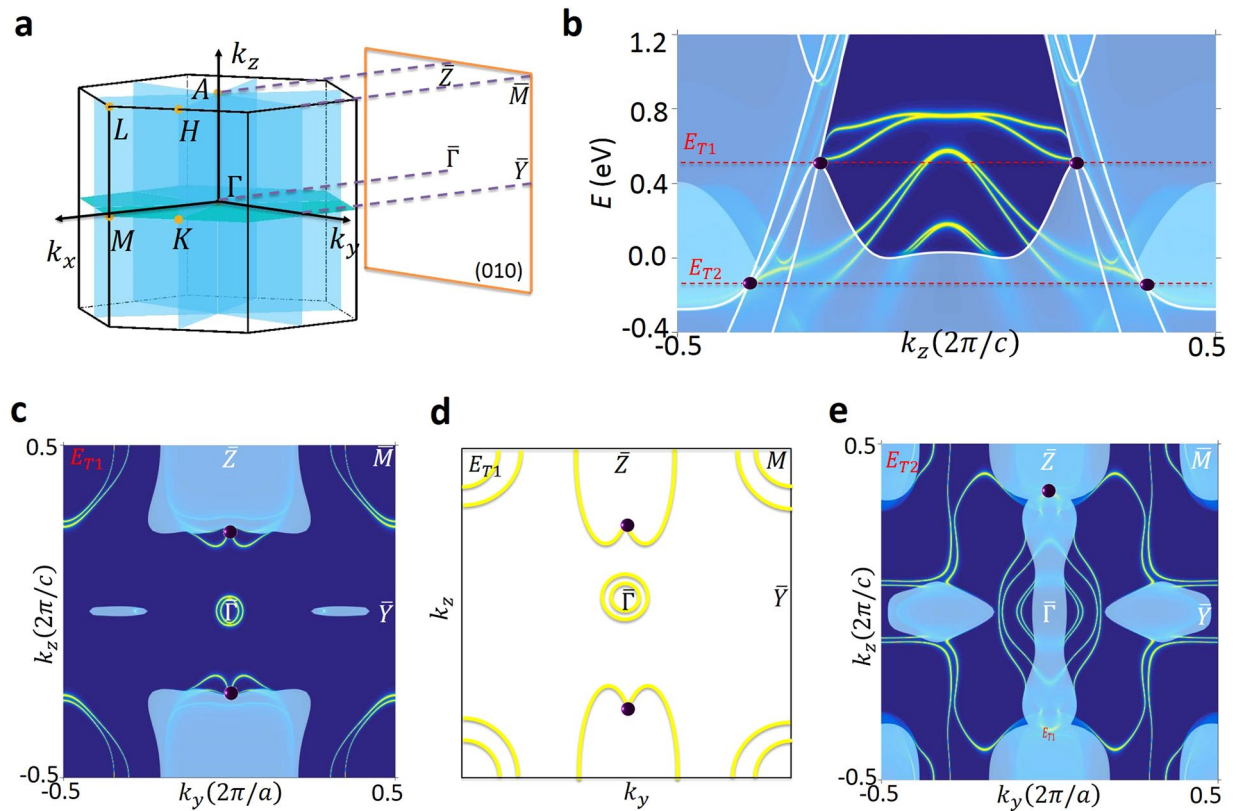


Figure 5. Topological surface states in the new TM. (a) The bulk BZ and the (100) surface BZ of WC. (b) Surface band structure along the k_z axis (the $\tilde{\Gamma} - \tilde{A}$ line). The white lines show the bulk bands, and the purple spheres denote the triply-degenerate nodes. (c,e) Surface constant energy contours at the energies of the two triply-degenerate nodes. (d) Schematic illustration of the surface state Fermi arc connectivity in WC.

present in the Weyl case. We can qualitatively understand these results by visualizing the triply-degenerate band crossing as a Weyl cone plus a third band. This can be clearly seen in the cartoon in Fig. 1d,e. For the Landau level structure, the green-blue cone acts like a Weyl cone, while the yellow surface is the third band. They overlap each other on a line that is along the k_z direction. The Landau level spectrum can be explained using this picture. While the Weyl cone will contribute its characteristic Landau level structure, additional Landau levels observed can be explained by the third band. Particularly, if the third band were like a completely flat surface, meaning that it has no dispersion along the in-plane k_x and k_y directions, then all additional bands would be degenerate with the zeroth chiral Landau level, and the zeroth chiral Landau level would have a huge degeneracy. In real materials, the third band will have finite in-plane dispersion. Hence the additional bands become non-degenerate with the zeroth chiral Landau level. This demonstrates that the Landau level spectrum of the triply-degenerate fermion is distinctly different from that of Weyl semimetals. This finding suggests novel magnetotransport responses and further demonstrates the exotic and unique properties of TMs with emergent triply-degenerate fermions.

Material realizations

We have determined the space groups in which the new TM state can occur and identified material candidates for each space group. Importantly, the material candidates that we identified cover both Class α/β and type I/II. The space groups include #187–#190 for Class α and #156–#159 for Class β . A list of the candidate materials is presented in Table 1. Here, we take the example of tungsten carbide, WC, as shown in Fig. 4. WC crystalizes in a hexagonal Bravais lattice, space group $P-6m2$ (#187). The unit cell is shown in Fig. 4a), which obviously breaks space-inversion symmetry. The crystal has the C_{3z} rotational symmetry and both horizontal (\mathcal{M}_z) and vertical (\mathcal{M}_x) mirror planes. Hence we expect the new band crossing to be Class α . Figures 4c,d show the first-principles calculated band structures without and with SOC. Triply-degenerate band crossings are seen in both cases. We discuss the band crossing in the presence of SOC in detail. Figure 4e, left panel, shows the zoomed-in energy dispersion of the band crossing along k_z . It can be seen that the doubly-degenerate band (the blue curve) crosses with two singly-degenerate bands (black curves) forming two triply-degenerate nodes. The right panel shows the in-plane (k_a) dispersion that goes through one of the triply-degenerate nodes, where we clearly see that three singly-degenerate bands cross each other at one point. Finally, in Fig. 4f, we show that the triply-degenerate nodes in WC indeed split into pairs of Weyl nodes of opposite chirality in the presence of a Zeeman coupling.

We now study the surface states of WC. We choose the (100) surface so that the triply-degenerate nodes are not projected onto the same k point on the surface. The color plot in Fig. 5b shows the surface state band structure

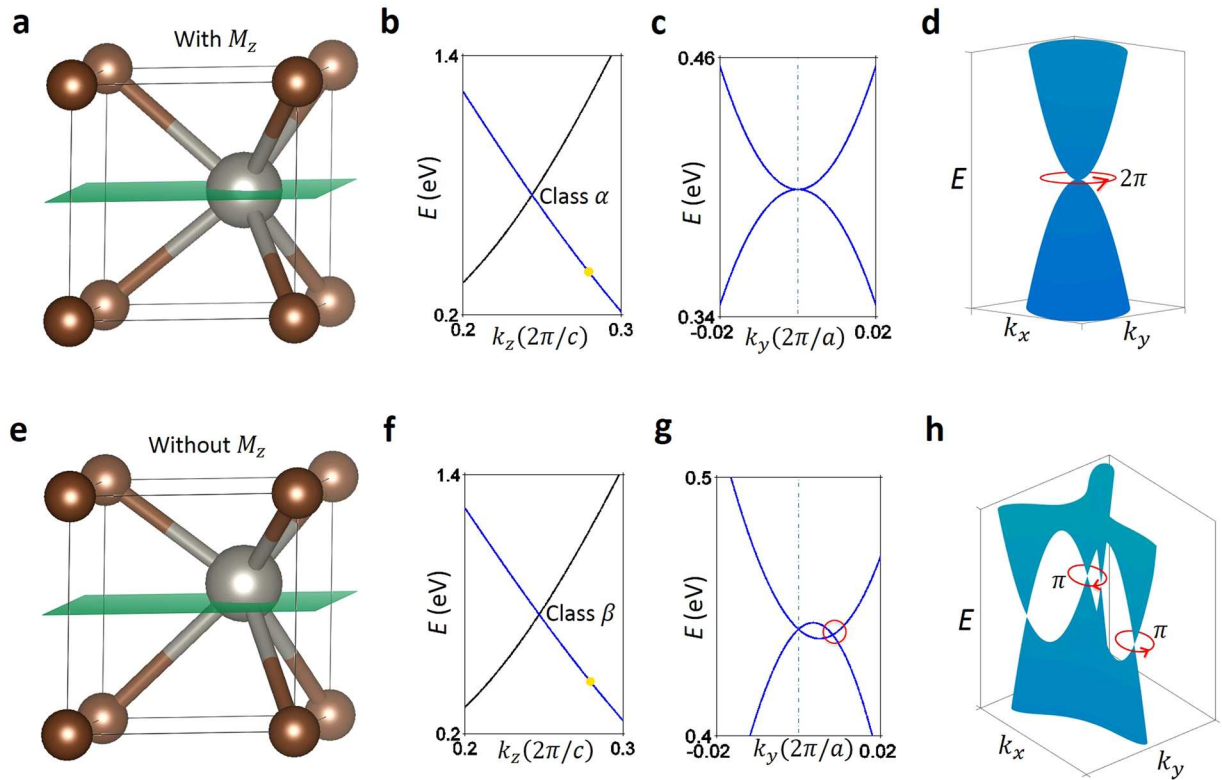


Figure 6. Transition from Class α to Class β by breaking \mathcal{M}_z mirror symmetry. (a) Crystal structure of WC with the W and C atoms represented by silver and bronze spheres and the $k_z=0$ (\mathcal{M}_z) mirror plane by a green plane. (b) Band structure along k_z and around the triply degenerate band crossing for Class α . The blue and black bands denote the doubly and singly degenerate bands, respectively. (c) At the location marked by the yellow dot in (b), we present the band dispersion of the doubly degenerate band along the in-plane k_y -direction. A quadratic dispersion for the ψ'_1 and ψ'_2 bands and a touching point between them is observed. The two bands are colored blue to signify they are from the doubly-degenerate band in (b). (d) A trivial Berry phase of 2π was computed for a closed loop around the touching point in (c). (e) The displacement of the W atom in (a) along the c lattice constant direction breaks the \mathcal{M}_z mirror symmetry. (f) Similar to (b), but for the broken \mathcal{M}_z mirror symmetry case. (g) Along a generic k_y direction, the doubly degenerate band is shown to have transitioned from Class α to Class β occurs through breaking the \mathcal{M}_z mirror symmetry. Specifically, the observed linearly dispersing touching points between ψ'_1 and ψ'_2 signifies the expected character of Class β . The red circle denotes one of the two linear touching points. (h) Illustration showcasing a non-trivial π Berry phase for a closed loop around the linearly dispersing touching points.

along the k_z direction (the $\tilde{\Gamma} - \tilde{A}$ line). We also superimpose the bulk bands (the white lines) along k_z onto this plot. We clearly see a pair of surface Fermi arcs emerging out of the triply-degenerate nodes with a higher energy ($T1$). On the other hand, because the lower triply-degenerate nodes ($T2$) are masked by other irrelevant bulk bands when projected onto the surface, we cannot tell whether they are also connected by the surface Fermi arcs. The constant energy contour map at energy $E=E_{T1}$ reveal the same phenomenon. That is, each triply-degenerate node is connected by two surface state Fermi arcs. We discuss a few essential aspects in connection to the arc character of the surface states: The Zeeman coupling effect shown in Figs. 3a–f shows that the triply-degenerate node splits into a pair of Weyl nodes of opposite chirality. From this angle, it makes sense that each triply-degenerate node is connected by a pair of Fermi arcs. Now, the question is that whether the arc character of the surface states is protected. Or in other words, whether the surface states are required to go through the triply-degenerate nodes. We know that the arc character is guaranteed in the case for Weyl semimetals because a Weyl node carry a net chiral charge. We also know that it is not guaranteed in Dirac semimetals because a Dirac node does not carry a net chiral charge⁴⁴. In our case, a definite conclusion is currently not possible because whether there exists a topological invariant for the triply-degenerate node is unknown. This is a highly valuable open question that requires further investigations in theory. On the other hand, one can define 2D topological invariants such as a mirror Chern number or a \mathbb{Z}_2 number on a 2D slice of the BZ as discussed above. Our calculation shows that the mirror Chern number $n_M = -1$ for the $k_z = \pi$ plane, indicating that there should be one surface state connecting the bulk band gap along the $\tilde{Z} - \tilde{M}$ segment. In Fig. 5d, we see three surface state along $\tilde{Z} - \tilde{M}$. Two of them that enclose the \tilde{M} point are trivial because they do not connect across the band gap. The third one, which is the Fermi arc that goes all the way from the triply-degenerate point to the $\tilde{Z} - \tilde{M}$ line is non-trivial. Therefore, the observed surface states are consistent with the $n_M = -1$ at $k_z = \pi$.

As was described in the discussion above, the distinguishing properties of Class α and Class β are understood to be a manifestation of the presence and absence of \mathcal{M}_z mirror symmetry, respectively. As shown in Fig. 6a, WC has a \mathcal{M}_z mirror symmetry plane at $k_z = 0$, which, according to its band structure around the triply degenerate band crossing shown in Fig. 6b, is of Class α . At a point away from the triply degenerate node but along the k_z -direction, the doubly degenerate band along k_y -direction, Fig. 6c, possess a quadratic band dispersion and touching point between the ψ'_1 and ψ'_2 bands. Now, by computing the Berry phase around a closed loop around the open segment, we observe a trivial 2π result, as shown in Fig. 6d. By now proceeding with breaking the \mathcal{M}_z mirror symmetry through shifting the W atom along the c -lattice constant direction, Fig. 6e, we observe that the two-fold degenerate 1D band crossings now form four strands at every cut of constant k_z , one of which is pinned to align with the k_z axis. Similar to before, by looking at the in-plane dispersion along k_y , the initial quadratic dispersion of the ψ'_1 and ψ'_2 bands and their touching point results in two linearly dispersing touching points in the absence of \mathcal{M}_z , as shown in Fig. 6g. By computing the Berry phase around the new touching points, enclosed by a red circle in Fig. 6h, we observe a non-trivial $\pm\pi$ value around each line. In the supplementary information (SI), we include band structure calculations of other Nexus fermion compounds.

In summary, the exploration of TMs has recently experienced a lot of progress and interest. While initially the attraction in TMs was amplified by the realization that the analogues of fermionic particles (e.g. Dirac, Weyl and Majorana fermions) in quantum field theory could be realized in a crystals k -space, we are now reaching a point in our understanding that is allowing the study of quasiparticle excitations arising from protected band crossings that do not have a direct analogy in the Standard Model. A crucial insight into the understanding in TMs is the importance of the band crossing dimensionality. While Weyl and Dirac semimetals have zero-dimensional points, the band crossing of nodal-line semimetals forms a one-dimensional closed loop. In this paper, we reported on a new TM that features a triply-degenerate band crossing thereby realizing quasiparticles that have no analog in quantum field theory. Furthermore, the band crossing is neither 0D or 1D, but a combination of both since the two isolated triply-degenerate nodes are interconnected by multiple segments of lines that are doubly-degenerate. We also present a list of crystalline candidate crystals that may realize this new TM. To further elucidate the distinguishing properties of this new three-fold degenerate band degeneracy, we performed detailed calculations on the material candidate WC and studied the Landau level spectrum arising from the node, which is distinct from Dirac and Weyl semimetals. Our results are not only pivotal to the development of our understanding of topological phases of quantum matter, but also provide suitable platforms to experimentally elucidate the transport anomalies and spectroscopic responses in these new TM crystals, which have nontrivial band topology that go beyond the Weyl/Dirac paradigm.

References

1. Turner, A. M. & Vishwanath, A. Beyond Band Insulators: Topology of Semi-metals and Interacting Phases. Preprint at <https://arxiv.org/abs/1301.0330> (2013).
2. Hasan, M. Z., Xu, S.-Y. & Neupane, M. Topological Insulators, Topological semimetals, Topological Crystalline Insulators, and Topological Kondo Insulators. In *Topological Insulators: Fundamentals and Perspectives* edited by Ortman, F., Roche, S. & Valenzuela, S. O. (John Wiley & Sons, 2015).
3. Hasan, M. Z., Xu, S.-Y. & Bian, G. Topological Insulators, Helical Topological Superconductors and Weyl Fermion Semimetals. *Phys. Scr.* **T164**, 014001, doi:[10.1088/0031-8949/2015/T164/014001](https://doi.org/10.1088/0031-8949/2015/T164/014001) (2015).
4. Xu, S.-Y. *et al.* Observation of Fermi arc surface states in a topological metal. *Science* **347**, 294–298, doi:[10.1126/science.1256742](https://doi.org/10.1126/science.1256742) (2015).
5. Huang, S. M. *et al.* A Weyl Fermion semimetal with surface Fermi arcs in the transition metal mononitride TaAs class. *Nature Commun.* **6**, 7373, doi:[10.1038/ncomms8373](https://doi.org/10.1038/ncomms8373) (2015).
6. Weng, H., Fang, C., Fang, Z., Bernevig, A. & Dai, X. Weyl semimetal phase in noncentrosymmetric transition metal monophosphides. *Phys. Rev. X* **5**, 011029 (2015).
7. Xu, S.-Y. *et al.* Discovery of a Weyl fermion semimetal and topological Fermi arcs. *Science* **349**, 613–617, doi:[10.1126/science.aaa9297](https://doi.org/10.1126/science.aaa9297) (2015).
8. Lu, L. *et al.* Observation of Weyl points in a photonic crystal. *Science* **349**, 622–624, doi:[10.1126/science.aaa9273](https://doi.org/10.1126/science.aaa9273) (2015).
9. Lv, B. Q. *et al.* Experimental Discovery of Weyl Semimetal TaAs. *Phys. Rev. X* **5**, 031013 (2015).
10. Xu, S.-Y. *et al.* Discovery of a Weyl Fermion semimetal state in NbAs. *Nature Phys.* **11**, 748–754, doi:[10.1038/nphys3437](https://doi.org/10.1038/nphys3437) (2015).
11. Soluyanov, A. A. *et al.* Type II Weyl Semimetals. *Nature* **527**, 495–498, doi:[10.1038/nature15768](https://doi.org/10.1038/nature15768) (2015).
12. Yu, Z., Yao, Y. & Yang, S. A. Unusual Magneto-Response in Type-II Weyl Semimetals. *Phys. Rev. Lett.* **117**, 077202 (2016).
13. Xu, S.-Y. *et al.* Discovery of Lorentz-violating Weyl fermion semimetal state in LaAlGe materials. Preprint at <http://arxiv.org/abs/1603.07318> (2016).
14. Chang, G. *et al.* Theoretical prediction of magnetic and noncentrosymmetric Weyl fermion semimetal states in the R-Al-X family of compounds (R = rare earth, Al = aluminium, X = Si, Ge). Preprint at <http://arxiv.org/abs/1604.02124> (2016).
15. Huang, X. *et al.* Observation of the Chiral-Anomaly-Induced Negative Magnetoresistance in 3D Weyl Semimetal TaAs. *Phys. Rev. X* **5**, 031023 (2015).
16. Xiong, J. *et al.* Evidence for the chiral anomaly in the Dirac semimetal Na3Bi. *Science* **350**, 413–416, doi:[10.1126/science.aac6089](https://doi.org/10.1126/science.aac6089) (2015).
17. Zhang, C. *et al.* Signatures of the Adler-Bell-Jackiw chiral anomaly in a Weyl semimetal. *Nature Commun.* **7**, 10735, doi:[10.1038/ncomms10735](https://doi.org/10.1038/ncomms10735) (2016).
18. Nielsen, H. B. & Ninomiya, M. The Adler-Bell-Jackiw anomaly and Weyl fermions in a crystal. *Physics Letters B* **130**, 389–396, doi:[10.1016/0370-2693\(83\)91529-0](https://doi.org/10.1016/0370-2693(83)91529-0) (1983).
19. Parameswaran, S. A. *et al.* Probing the chiral anomaly with nonlocal transport in three-dimensional topological semimetals. *Phys. Rev. X* **4**, 031035 (2014).
20. Potter, A. C., Kimchi, I. & Vishwanath, A. Quantum oscillations from surface Fermi-arcs in Weyl and Dirac semi-metals. *Nature Commun.* **5**, 5161, doi:[10.1038/ncomms6161](https://doi.org/10.1038/ncomms6161) (2014).
21. Baum, Y., Berg, E., Parameswaran, S. A. & Stern, A. Current at a Distance and Resonant Transparency in Weyl Semimetals. *Phys. Rev. X* **5**, 041046 (2015).
22. Kargarian, M., Randeria, M. & Trivedi, N. Theory of Kerr and Faraday rotations and linear dichroism in Topological Weyl Semimetals. *Sci. Rep.* **5**, 12683, doi:[10.1038/srep12683](https://doi.org/10.1038/srep12683) (2015).
23. Murakami, S. & Nagaosa, N. Berry phase in Magnetic Superconductors. *Phys. Rev. Lett.* **90**, 057002, doi:[10.1103/PhysRevLett.90.057002](https://doi.org/10.1103/PhysRevLett.90.057002) (2003).

24. Hosur, P. & Qi, X.-L. Time-reversal invariant topological superconductivity in doped Weyl semimetals. *Phys. Rev. B* **90**, 045130, doi:[10.1103/PhysRevB.90.045130](https://doi.org/10.1103/PhysRevB.90.045130) (2014).
25. Li, Y. & Haldane, F. D. M. Topological nodal Cooper pairing in doped Weyl semimetals. Preprint at <http://arxiv.org/abs/1510.01730> (2015).
26. Kim, Y., Park, M. J. & Gilbert, M. J. Probing unconventional superconductivity in inversion symmetric doped Weyl semimetal. <http://arxiv.org/abs/1604.01040> (2016).
27. Wieder, F., Kim, Y., Rappe, A. M. & Kane, C. L. Double Dirac Semimetals in Three Dimensions. *Phys. Rev. Lett.* **116**, 186402, doi:[10.1103/PhysRevLett.116.186402](https://doi.org/10.1103/PhysRevLett.116.186402) (2016).
28. Bradlyn, B. *et al.* New Fermions. Preprint at <http://arxiv.org/abs/1603.03093> (2016).
29. Volovik, G. E. *The Universe in a Helium Droplet* (Oxford University Press, 2003).
30. Heikkilä, T. T. & Volovik, G. E. Nexus and Dirac lines in topological materials. *New J. Phys.* **17**, 093019, doi:[10.1088/1367-2630/17/9/093019](https://doi.org/10.1088/1367-2630/17/9/093019) (2015).
31. McCann, E. & Koshino, M. The electronic properties of bilayer graphene. *Rep. Prog. Phys.* **76**, 056503, doi:[10.1088/0034-4885/76/5/056503](https://doi.org/10.1088/0034-4885/76/5/056503) (2013).
32. Page, K. *et al.* Reciprocal-space and real-space neutron investigation of nanostructured Mo₂C and WC. *Solid State Sciences* **10**, 1499–1510, doi:[10.1016/j.solidstatesciences.2008.03.018](https://doi.org/10.1016/j.solidstatesciences.2008.03.018) (2008).
33. Örlýgsson, G. & Harbrecht, B. The Crystal Structure of WC Type ZrTe. Advantages in Chemical Bonding as Contrasted to NiAs Type ZrTe. *Zeitschrift für Naturforschung B* **54**, 1125–1128, doi:[10.1515/znb-1999-0906](https://doi.org/10.1515/znb-1999-0906) (1999).
34. Fontbonne, A. & Gilles, J. C. Nouveaux nitrures de tantale. Nitrure et oxynitrures mixtes de tantale et de niobium. *Rev. Int. Hautes* **6**, 181–192 (1969).
35. Schönberg, N. The tungsten carbide and nickel arsenide structures. *Acta Metallurgica* **2**, 427–432, doi:[10.1016/0001-6160\(54\)90062-0](https://doi.org/10.1016/0001-6160(54)90062-0) (1954).
36. Ravi, C. First-principles study of ground-state properties and phase stability of vanadium nitrides. *Calphad* **33**, 469–477, doi:[10.1016/j.calphad.2009.03.001](https://doi.org/10.1016/j.calphad.2009.03.001) (2009).
37. Lachgar, A. *et al.* Synthesis and properties of two novel line phases that contain linear scandium chains, LiScI₃ and Na_{0.5}ScI₃. *Inorg. Chem.* **30**, 3321–3326, doi:[10.1021/ic00017a019](https://doi.org/10.1021/ic00017a019) (1991).
38. Christensen, A. N. & Lebech, B. A reinvestigation of the structure of ϵ -tantalum nitride. *Acta Crystallographica Section B: Structural Crystallography and Crystal Chemistry* **34**, 261 (1978).
39. Müller, W. Notizen: Darstellung und Struktur der Phase Li₂Sb Preparation and Crystal Structure of Li₂Sb. *Zeitschrift für Naturforschung B* **32**, 357, doi:[10.1515/znb-1977-0326](https://doi.org/10.1515/znb-1977-0326) (1977).
40. Range, K. J., Engert, G. & Weiss, A. Darstellung und Kristallstruktur der Hochdruckphase AgAlS₂-II/Preparation and Crystal Structure of the High-pressure Phase AgAlS₂-II. *Zeitschrift für Naturforschung B* **29**, 186 (1974).
41. Alasafi, K. M. & Schubert, K. Kristallstruktur von AuCd. *Journal of the Less Common Metals* **55**, 1–8, doi:[10.1016/0022-5088\(77\)90255-7](https://doi.org/10.1016/0022-5088(77)90255-7) (1977).
42. Fletcher, J. M. *et al.* X-Ray, infrared, and magnetic studies of α - and β -ruthenium trichloride. *Journal of the Chemical Society A: Inorganic, Physical, Theoretical* **1038** (1967).
43. Ruddlesden, S. N. & Popper, P. On the crystal structure of the nitrides of silicon and germanium. *Acta Crystallographica* **11**, 465–468, doi:[10.1107/S0365110X58001304](https://doi.org/10.1107/S0365110X58001304) (1958).
44. Yang, B.-J. & Nagaosa, N. Classification of stable three-dimensional Dirac semimetals with nontrivial topology. *Nature Commun.* **5**, 4898, doi:[10.1038/ncomms5898](https://doi.org/10.1038/ncomms5898) (2014).

Acknowledgements

Work at Princeton University was supported by the U.S. Department of Energy (DOE), Office of Science, Basic Energy Sciences (BES), under DE-FG-02-05ER46200. Work at the National University of Singapore was supported by the National Research Foundation (NRF), Prime Minister's Office, Singapore, under its NRF fellowship (NRF award no. NRFNRF2013-03). T.-R.C. and H.-T.J. were supported by the National Science Council, Taiwan. H.-T.J. also thanks the National Center for High-Performance Computing, Computer and Information Network Center, National Taiwan University, and the National Center for Theoretical Sciences, Taiwan, for technical support. Work at Northeastern University was supported by U.S. DOE/BES grant no. DE-FG02-07ER46352 and benefited from Northeastern University's Advanced Scientific Computation Center and the National Energy Research Scientific Computing Center supercomputing center through DOE grant no. DE-AC02-05CH11231. S.M.H., G.C., and T.R.C. acknowledge their visiting scholar positions at Princeton University, which were funded by the Gordon and Betty Moore Foundation EPiQS Initiative through grant GBMF4547 (Hasan).

Author Contributions

All authors contributed to the intellectual contents of this work. Preliminary material search and initial design of the prediction were done by S.-Y.X. and G.C. with help from all authors. The band structure calculations were then performed by G.C., S.-M.H., C.-H.H., T.-R.C., H.-T.J., H.L.; Theoretical analysis were done by G.-C., S.-M.H., T.N., and H.L.; Landau level calculations were performed by Z.-M.Y. and S.A.Y.; G.C., S.-Y.X., T.N., D.S.S., G.B., I.B., N.A., H.Z., H.L., and M.Z.H. wrote the manuscript; S.-Y.X., H.L. and M.Z.H. were responsible for the overall research direction, planning and integration among different research units.

Additional Information

Supplementary information accompanies this paper at doi:[10.1038/s41598-017-01523-8](https://doi.org/10.1038/s41598-017-01523-8)

Competing Interests: The authors declare that they have no competing interests.

Publisher's note: Springer Nature remains neutral with regard to jurisdictional claims in published maps and institutional affiliations.



Open Access This article is licensed under a Creative Commons Attribution 4.0 International License, which permits use, sharing, adaptation, distribution and reproduction in any medium or format, as long as you give appropriate credit to the original author(s) and the source, provide a link to the Creative Commons license, and indicate if changes were made. The images or other third party material in this article are included in the article's Creative Commons license, unless indicated otherwise in a credit line to the material. If material is not included in the article's Creative Commons license and your intended use is not permitted by statutory regulation or exceeds the permitted use, you will need to obtain permission directly from the copyright holder. To view a copy of this license, visit <http://creativecommons.org/licenses/by/4.0/>.

© The Author(s) 2017